

SPATIOTEMPORAL ANALYSIS BASED ON SAR SATELLITE AND FIELD DATA RELATED TO DECLINING OF GEOTHERMAL PRODUCTION IN WEST JAVA, INDONESIA.

5.1. INTRODUCTION

Characterizing physical properties of ground surface based on Synthetic Aperture Radar (SAR) are crucial for geological target detection under Torrid Zone condition (Saepuloh et al., 2010). The backscattering intensity of SAR chiefly a function of two physical quantities of surface material, the surface roughness and dielectric parameters. The two parameters were proved effective to discriminate ground surface materials at volcanic field such as pyroclastic flows, lava, and lahars (Saepuloh et al., 2010). In this research, we focused to obtaining surface parameter related to the permeability based on Polarimetric SAR (PolSAR) data. The surface permeability is a crucial parameter for estimating geothermal potential. Furthermore, analyzing spatiotemporal of surface permeability will be important to understand the dynamic of fluid extraction in geothermal power plant and the effect of declining of geothermal production. In the exploitation stage, monitoring of production wells is the most important activity in maintaining and increasing steam production in a geothermal field.

Various method of monitoring are used, one of the methods used includes an in-depth analysis of various data such as geological, geochemical, geophysical data, and remote sensing. In the stage of exploitation and field development, the survival and sustainability of production wells in generating energy is a very important part. This monitoring activity needs to be done, not only at the point of production wells, but also the surrounding areas because the coverage area of geothermal system is wide. Field measurement data can be used as a reference in monitoring of production, but the data only available in certain points or areas. Data of the field measurement is limited, and monitoring of production areas is hard to do so, especially in areas outside of production wells. This will lead to poor supervision or delay in response to engineered wells that have decreased production. To solve this problem, we propose a study to analyze changes in surface permeability associated with spatiotemporal geothermal pathways using the active remote sensing method of Polarimetric SAR (PolSAR) and Interferometric SAR (InSAR) data related to steam production in the geothermal field. This SAR data has proven to be effective in tropical regions such as Indonesia because of its ability to penetrate clouds as well as vegetation canopy (Saepuloh et al., 2012). Figure 1. Show the location of study area at Wayang windu Geothermal Field (WWGF). Geographically located at (778000 – 800000) mE and (9195000 – 9215000) mN with zone 48S UTM. Administratively, this geothermal field is included in Pangalengan District, Bandung Regency, West Java, Indonesia.

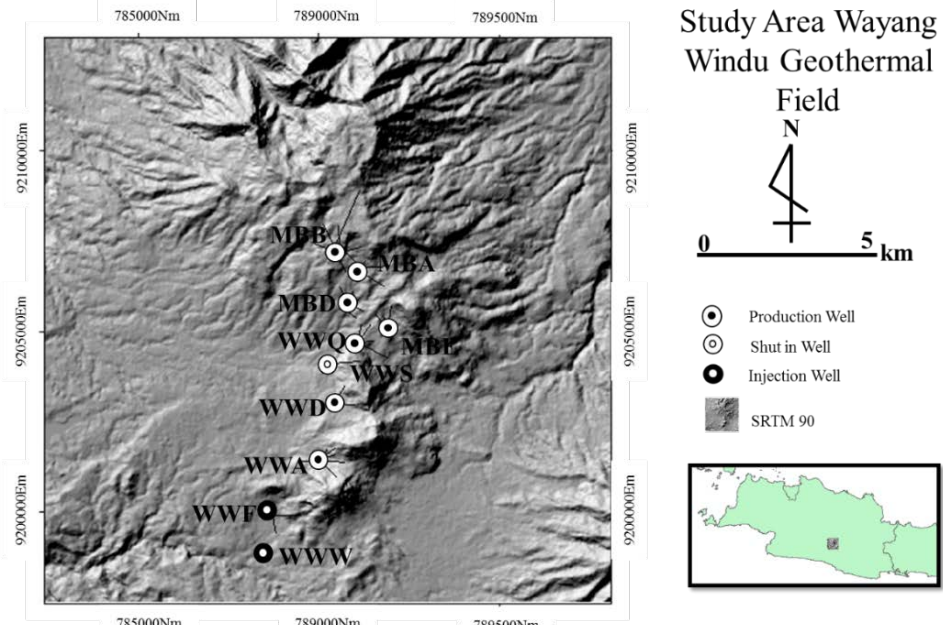


Figure 1. Study area located at Wayang Windu Geothermal Field (WWGF) overlaid on shaded map SRTM 90 m. Production and injection wells are presented by black and white dots, respectively.

WWGF is composed by ongoing production wells including MBA1, MBA2, MBA3, MBA4, MBA5, MBB1, MBB2, MBB3, MBB4, MBB5, MBD1, MBD2, MBD3, MBD4, MBD5, MBE3, WWA4, WWA6, WWD1, WWQ3 and WWQ5 and three injection wells located at south of the area including WWW2, WWF1 and WWF3. They have also shutted in well including MBE4, WWA2, WWA3, WWA5, WWD2, WWQ2, WWQ4 and WWS1. The production wells in WWGF produce steam with common phenomenon declining 6% annually. Some factors including engineering and geothermal system may influence to the declining. The spatial change detected by SAR images were aimed to interpret the cause of declining production in WWGF. The position of injections wells was also observed to predict the influence of the injected water to the geothermal system in view point of surficial changes detected by SAR images. Therefore, the amount of extracted and injected fluid from and to the system was subjected to the change of physical properties of ground surface.

5.2. ALOS PALSAR DATA SERIES

The analysis of spatiotemporal in this research covered 4 years at selected location including surface manifestation, production, and injection wells. The ALOS PALSAR data ascending-descending orbits were used with acquisition date (6/10/2007) until (3/21/2011). The 18 pairing data in ascending-descending were selected to extract lineaments related to fault and fractures at ground surface. Selecting region of interest to only WWGF area was used to optimize the result and reducing time processing. The ALOS PALSAR ascending and descending orbit in WWGF could be identified by the last two digit number from the Scene ID that number 40 and 60 are ascending and descending orbit, respectively. The ascending-descending data have spatial resolution in range and azimuth 30.68 m × 30.72 m. Details ALOS PALSAR data used in this research are listed at Table 1.

The azimuth bias is a common phenomenon which caused by an oblique SAR sensor orthogonal to the satellite track. The topographical structures oriented approximately north-south are selectively enhanced, whilst those oriented approximately east-west are selectively degraded (Smith and Wise, 2007). In order to reduce the effects of azimuth biasing, we used two scenes of ALOS PALSAR data in ascending and descending orbits as listed in Table 1. The ALOS PALSAR is a sun-synchronous polar satellite with repeat cycles 46 days possible to observe the ground surface in different LOS termed as ascending and

descending. The ascending and descending orbits indicated the azimuth of the sensor from north heading south with LOS to the east and from south heading north with LOS to the left, respectively. The dual orbit images are superior to resolve weak backscattering signal from the back slope. Therefore, the low contrast of the lineaments due to depression angle of the sensor could be observed as well.

Table 1. ALOS PALSAR Data used in this research.

No	Scene ID	Orbits	Acquisition Date	Resolution (Rg×Az)
1	ALPSRP073233760	Descending	6/10/2007	(30.68×30.72) m
2	ALPSRP078707040	Ascending	7/17/2007	(30.68×30.72) m
3	ALPSRP085417040	Ascending	9/1/2007	(30.68×30.72) m
4	ALPSRP086653760	Descending	9/10/2007	(30.68×30.72) m
5	ALPSRP092127040	Ascending	10/17/2007	(30.68×30.72) m
6	ALPSRP093363760	Descending	10/26/2007	(30.68×30.72) m
7	ALPSRP098837040	Ascending	12/2/2007	(30.68×30.72) m
8	ALPSRP100073760	Descending	12/11/2007	(30.68×30.72) m
9	ALPSRP105547040	Ascending	1/17/2008	(30.68×30.72) m
10	ALPSRP106783760	Descending	1/26/2008	(30.68×30.72) m
11	ALPSRP125677040	Ascending	6/3/2008	(30.68×30.72) m
12	ALPSRP126913760	Descending	6/12/2008	(30.68×30.72) m
13	ALPSRP132387040	Ascending	7/19/2008	(30.68×30.72) m
14	ALPSRP133623760	Descending	7/28/2008	(30.68×30.72) m
15	ALPSRP139097040	Ascending	9/3/2008	(30.68×30.72) m
16	ALPSRP140333760	Descending	9/12/2008	(30.68×30.72) m
17	ALPSRP145807040	Ascending	10/19/2008	(30.68×30.72) m
18	ALPSRP147043760	Descending	10/28/2008	(30.68×30.72) m
19	ALPSRP152517040	Ascending	12/4/2008	(30.68×30.72) m
20	ALPSRP153753760	Descending	12/13/2008	(30.68×30.72) m
21	ALPSRP159227040	Ascending	1/19/2009	(30.68×30.72) m
22	ALPSRP160463760	Descending	1/28/2009	(30.68×30.72) m
23	ALPSRP186067040	Ascending	7/22/2009	(30.68×30.72) m
24	ALPSRP187303760	Descending	7/31/2009	(30.68×30.72) m
25	ALPSRP219617040	Ascending	3/9/2010	(30.68×30.72) m
26	ALPSRP220853760	Descending	3/18/2010	(30.68×30.72) m
27	ALPSRP226327040	Ascending	4/24/2010	(30.68×30.72) m
28	ALPSRP227563760	Descending	5/3/2010	(30.68×30.72) m
29	ALPSRP234273760	Descending	6/18/2010	(30.68×30.72) m
30	ALPSRP239747040	Ascending	7/25/2010	(30.68×30.72) m
31	ALPSRP246457040	Descending	9/9/2010	(30.68×30.72) m
32	ALPSRP254403760	Descending	11/3/2010	(30.68×30.72) m
33	ALPSRP259877040	Ascending	12/10/2010	(30.68×30.72) m
34	ALPSRP261113760	Descending	12/19/2010	(30.68×30.72) m
35	ALPSRP273297040	Ascending	3/12/2011	(30.68×30.72) m
36	ALPSRP274533760	Descending	3/21/2011	(30.68×30.72) m

5.3. GROUND SURFACE CONDITION AT STEAM FIELDS

The physical parameters at and around ground surface of geothermal manifestation were measured to estimate the surface permeability spatially. The measurements were consisted of ground pH, magnetic

susceptibility, electric conductivity, and surface roughness. The acidity parameter presented by ground pH lower than 7 is one parameter to identify geothermal surface manifestation (Gherardi et al., 2002; Joseph et al., 2013; Libbey and Williams-Jones, 2016). Furthermore, the measured physical parameters will be used to assess the effectiveness of detected lineaments and their densities based on mSTA method as explained in the following section. The measured points are following the clustered pattern with lag distance about 30 m for each cluster in general. There are 16 clusters in total consisting 9 clusters at geothermal surface manifestation and 7 clusters out from geothermal surface manifestation. Four clusters were measured at altered surfaces, one cluster at mud pools, and four clusters at hot springs.

According to Saepuloh et al. (2016), there is no gradational pH in spatial boundary of surface manifestation because of local distribution and controlled by surface permeability. For altered surface clusters, the geothermal fluids affected to the rock matrices higher than rock fragments. Therefore, the altered rock matrices are easier to be eroded than rock fragments. The field observation confirmed that the ground surfaces are covered chiefly by rock fragments with size from gravel to boulder (Figure 2 photograph 4th). Low pH caused strong alteration to the matrices of lava and pyroclastics which produced rough surfaces of rock fragments. On the contrary, high pH affects the rock surfaces relatively weak for same geological condition. For mud pools, the smooth and rough surfaces agreed with low and high pH, respectively. The ground surfaces mud pools cluster is covered by rare vegetation such as grasses, farms, and trees (Figure 2 photograph 1st). The cluster located at a crater with diameter about 350 m is bordered by abrupt topographic at NE part and located in the valley with a flat surfaces (Figure 2 photograph 4th). Based on field condition, the weathering is more influence to the ground surfaces than alteration process. The weathering process changes the rock matrices and fragments to soil. Therefore, the ground surface is flat without fragmental material such as gravel and boulder.

For hot springs clusters, the ground surfaces mainly are covered by grasses, tea plantations, and farms. The hot springs is located at wet ground and ponds with undulated topography. The temperature and pH of the warm ponds are about 55° C and 6.3, respectively. The hot springs might affect the host rocks weakly. Therefore, the surface roughness is independently to the spatial effect of the hot springs. According to the geological map (Alzwar et al., 2004), the hot springs clusters are mainly composed by laharic deposits containing fine to coarse old volcanic products. The weak and limited hydrothermal activities to large fragmented materials might cause low correlation between pH and the surface roughness (Figure 2 photograph 2nd and 3rd). According to characteristics of the surface roughness at three geothermal manifestation clusters, the altered surfaces and mud pools have correlation to the roughness of their ground surfaces (Saepuloh et al., 2016). The rock types and thermal activities are supposed to be the significant to the ground surface processes. Strong thermal activities will alter the matrices of hard volcanic products such as lava flow and pyroclastics into high erodability material such as clays. Then, the erosion process removes the matrices and remains the fragments of the rocks. Therefore, the surface roughness will be high. However, when the high thermal activities interact with soft volcanic products such as tuff and lahar, the surface erodability will be high which produces flat surfaces. It may infer that the low thermal activities will affect the volcanic products weakly.

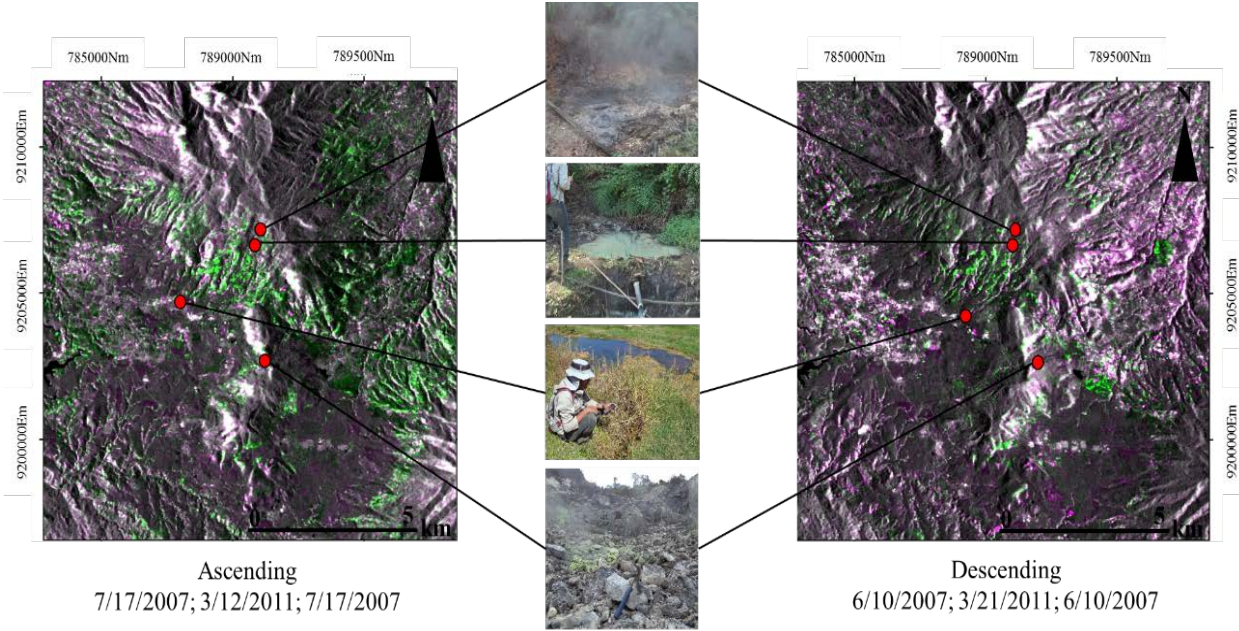


Figure 2. Color composite of ALOS PALSAR backscattering intensity image for R,G,B = 7/17/2007, 3/12/2011, 7/17/2007 showed surficial changes over time. The three subsets are locations of geothermal manifestation including mud pools, altered surfaces, and hot springs.

Based on the groundtruth and relating with the result of color composite with acquisition date 7/17/2007 for R and B, 3/12/2011 for G. Some of the area presented volume scattering originated from vegetated area and signed by green portion. The Wayang crater (Figure 3A) presented altered surfaces was located at bright tone in the image. The color composite result between ascending and descending data presented much better in true color composite than descending data. Manifestation at Kawah Burung mud pool and hot spring (Figure 3B) cannot be detected clearly from color composite due to limitation of spatial resolution. On the contrary, the hot spring at Kertamanah (Figure 3C) presented by dark tone due to flat terrain surrounding farmland.

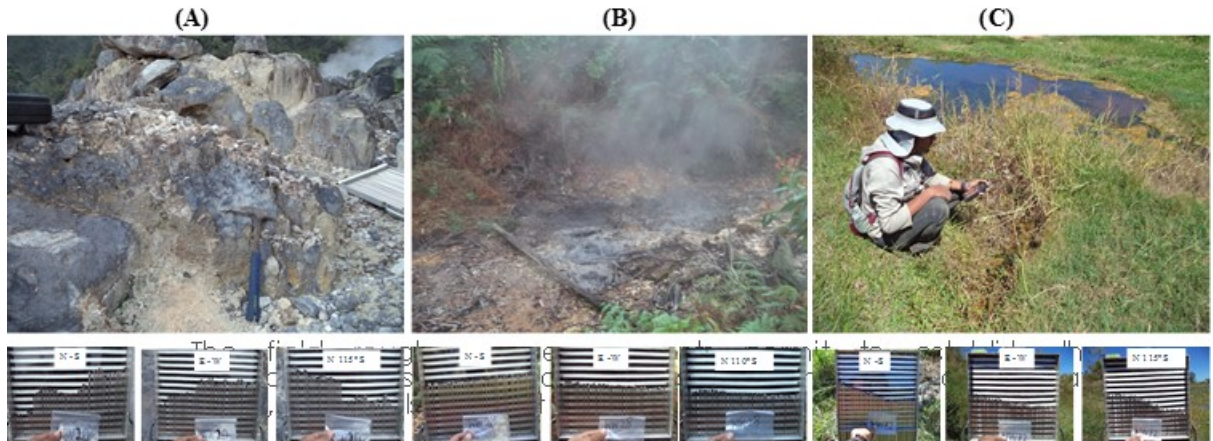


Figure 3. Measured geothermal surface manifestations at altered surfaces [A], mud pools [B], and hot springs [C] using magnetic susceptibility, electric conductivity, pH, and pin meters.

5.4. LINEAMENT DENSITY FROM MODIFIED SEGMENT TRACING ALGORITHM (MSTA)

The methodology to be used in this research involves the detection of surface permeability related to fault and fractures density using ALOS PALSAR dual orbits data and surface deformation using PS-

InSAR method. Pre-processing for SAR data covering radiometric and geometric correction. Radiometric correction is performed to increase the ratio of Signal to Noise (SNR), while geometry correction is necessary to obtain the position of the image pixel at the appropriate location. In addition, this correction is also to improve the image distortion due to the SAR data acquisition process is tilted or off nadir. The detection is based on ground surface physical measurement data at the surface manifestation zone in the geothermal field. Surface physical approaches such as surface roughness and electrical constants are used to detect surface permeability of a geothermal system. After that, a temporal analysis is conducted to determine the changes occurring around the geothermal production area

Geomorphologic and Structural Features (GSF) with SAR data is very effective for identifying the limits of rock units and surface geological structures (Saepuloh et al., 2012). An automated extraction method termed as Linear features density from Synthetic Aperture Radar (lifedSAR) was used to quantify the lineament of the SAR data associated with the geological structures (Saepuloh et al., 2013). The identification of surface geological structures is useful for mapping the surface permeability of a geothermal system. The lineament were detected automatically using modified of Segment Tracing Algorithm (mSTA) under MATLAB script. The advantage of this method is to extract linear features in the area with a low gray level. The backscattering intensities of ALOS PALSAR in ascending and descending orbits were used as basis of detection process. Following the linear features detection, the detected linear features were evaluated using vector summations to remove noises. The vector summations were aimed to eliminate the double-detected linear features in ascending or descending images due to hill-shade effect in high topography. Figure 3 showed up that the density of lineament from scene pair 1st ascending-descending until pair 18th are high dense. The high dense of lineament have similarity location with the faults distribution.

Lineaments are the main target in the SAR backscattering intensity images for identifying geological structures such as fault, joint, fractures, and breccia. Since the SAR sensors observe the ground surface in off-nadir, the lineaments were identified clearly especially for the structures with perpendicular to the range direction. The lineaments were identified as contrast texture and shading in the images. The Segment Tracing Algorithm (STA) is an effective technique to identify lineaments based on multi-shading images from DEM data (Koike et. al., 1995; 2001). Lineaments extraction based on grouping process in the STA were applied to remove the noise in the DEM and optical sensor data (Koike et al., 2001; Masoud and Koike, 2011b). Therefore, the modification of the STA is required to fit with different input and to improve the detection accuracy as follows:

Step 1. Linear feature element identification using search window 11×11 pixels around a centre pixel. The sixteen directions with 11.25° intervals passing through the centre of the window were defined to examine a local variation of grayscale along each line. The examples of line directions through a centre pixel within search window is depicted by Figure 4. The lineaments were selected by minimizing the ε_j as follows:

$$\varepsilon_j = \sum_{i=-a}^a w_i (Z^* - Z_i)^2, \quad w_i = \cos\left(\frac{i\pi}{4a}\right) \quad \text{for } j = 1, \dots, 16 \quad (1)$$

where Z^* is the gray scale of the centered pixel, w_i is the weight coefficient to emphasize the difference in grayscale of the centered pixel and its neighboring pixel, and a is set to 5. The direction with ε_j minima were stored as member of K_{min} . The criterion to select the most appropriate lineaments was improved to the previous STA method for the stored K_{min} is only 1, then j is assumed to be the valley and the k_{min} is selected. However, in the most cases in the backscattering SAR images the stored K_{min} is more than 1, so that appropriate lineaments were selected based on average minima E_j as follows:

$$E_j = \frac{\varepsilon_{j-1} + \varepsilon_j + \varepsilon_{j+1}}{3} \quad \text{for } j \in K_{\min} \quad (2)$$

The selected direction which minimizes the value of E expressed by j is member of k_{\min} .

Step 2. Defining a grayscale at location x by $Z(x)$. Along the direction perpendicular to k_{\min} termed as k_{max} , squared secondary differentiation for grayscale, λ , was calculated by:

$$\Lambda = \sum_{i=-(a-1)}^{a-1} \lambda_i = \sum_{i=-(a-1)}^{a-1} \left[\frac{(Z_{i+1} - 2Z_i + Z_{i-1})^2}{Z_i} \right] \quad (3)$$

Expressing the mean and standard deviation of λ by m and σ , a dynamic threshold T defined as:

$$T = m + \mu\sigma, \quad \mu = \phi_1((1 + \sin \theta)^{-1} - 0.5) \quad (4)$$

where θ is the included angle between the sun's azimuth (s_p) and k_{max} , and ϕ_1 is a constant. The lineaments element that lie in the closest direction of s_p have a lowest threshold level. If the value calculated at the centered pixel of the window is above the threshold, the pixel is retained as a lineaments element (p).

Step 3. Judging whether p represents a ridge or valley features and p is eliminated when distributed at a ridge.

Step 4. Connecting the line elements. The distance between p and connectable pixels examined within the distance D from p could be expressed as follows:

$$D = \phi_2(1 + \sin \theta^*)^{-1} + \theta_3 \quad (5)$$

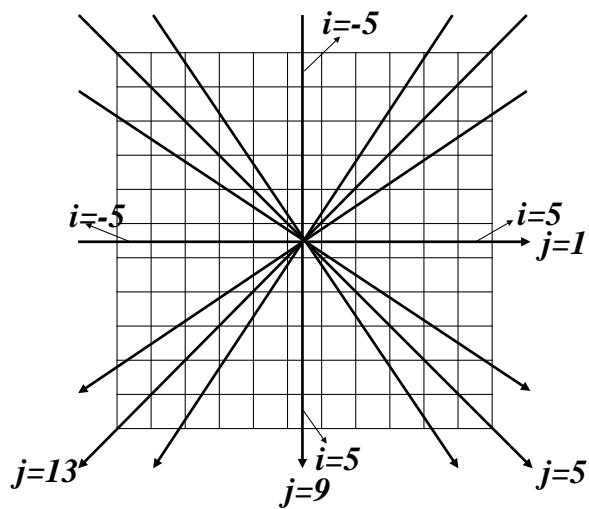


Figure 4. Illustration of k_{min} criterion for same minimum ε_j in search window 11×11 .

where θ^* is the included angle between the s_p and the k_{min} and ϕ_2 and ϕ_3 are constants. The value D is a dynamic threshold such that two pixels lying parallel to s_p and having a larger distance could be connected.

Step 5. A centerline for the line elements, which have similar directions and intersect each other is obtained from the (x, y) coordinates of the line elements using Principal Component Analysis.

The advantage of mSTA method is to extract lineaments in the area with a low gray level. The backscattering intensities of ALOS PALSAR in ascending and descending orbits were used as basis of detection process. Following the lineaments detection, the detected lineaments were evaluated using vector summations to remove noises. The vector summations were aimed to eliminate the double-detected lineaments in ascending or descending images due to hill-shade effect in high topography. Figure 5 shows detected lineament in series using vector summation from the ALOS PALSAR descending image. The lineament segments are distributed chiefly in the hill-shade. Some of the features probably originated from the geomorphologic pattern from erosional process. After the noise removal process, then the counted lineaments were reduced and the remaining is the detected targets. Finally, the lineaments obtained from ascending and descending images were combined. The similar direction and location of lineaments from the two images were removed to avoid the ambiguity (Figure 5).

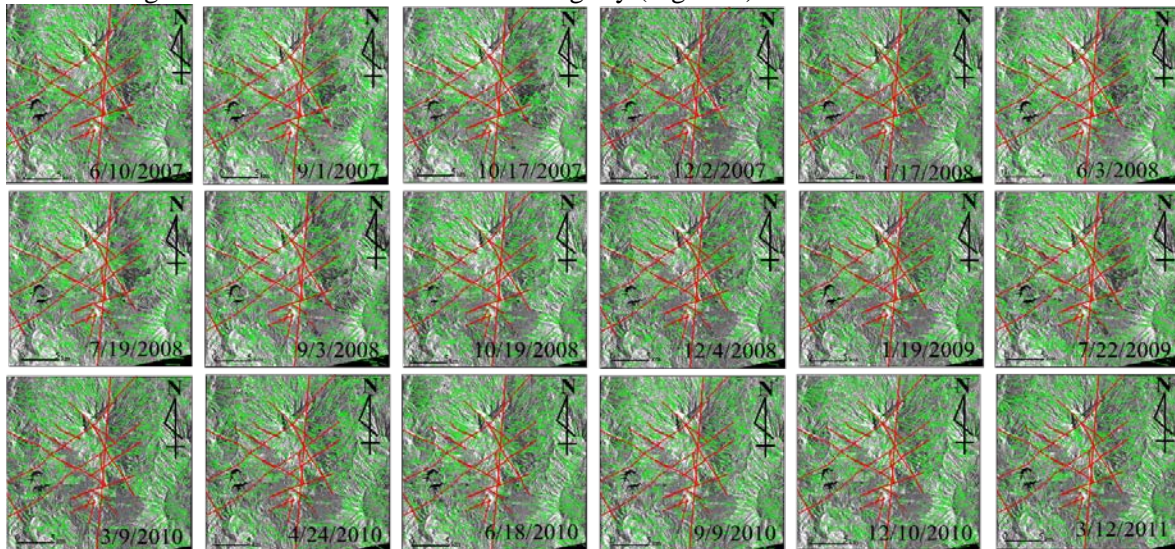


Figure 5. Time series of extracted lineaments based on mSTA overlaid with faults distribution in red lines of WWGF.

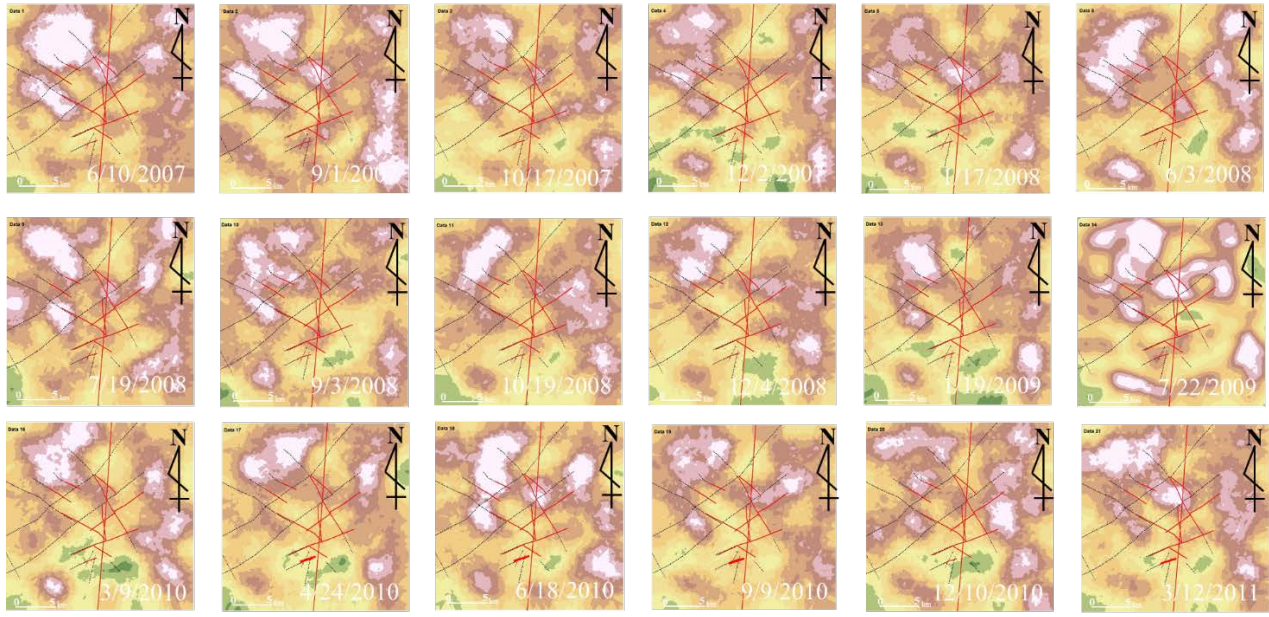


Figure 6. Lineament length density L_1 map series overlaid with fault distributions in WWGF.

The detected lineaments presented by Figure 5 were then quantified by dividing the study area into grids. The lineaments for each grid size termed as density are basis for surface permeability estimation. The density quantification leads a problem which density parameter and grid size are the most effective to estimate surface permeability. Overcoming the problem, we quantified the density 1×1 km grid for the linemanet length L_1 (km/km^2). The 1×1 km was selected as an effective grid size for geothermal study following Soengkono (1999). The densities for the three parameters were calculated for 24×24 km ($=576 \text{ km}^2$) covering study area. We applied a geostatistical approach based on Ordinary Kriging (OK) to map the L_1 . The variogram analysis was used as condition for spatial mapping based on OK. The variogram was fitted by a spherical model with omni-directional.

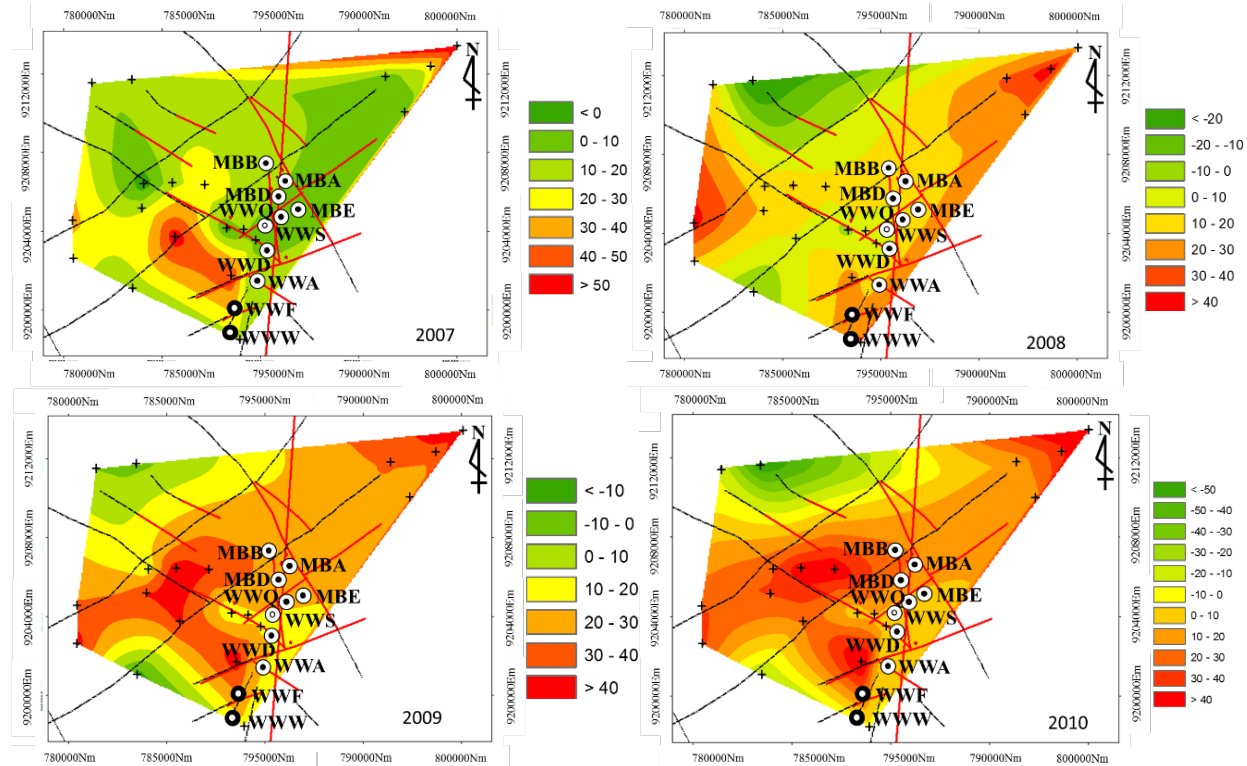
Fracture permeability is a key parameter for geothermal exploration. The fracturing zones at surface could be associated with dense lineaments. We used the density of L_1 after OK as a basis to estimate the surface permeability. The field measurements of surface manifestation were used as criterion for high surface permeability. The locations of field measurements presented by green dots were overlaid on the OK for L_1 density in Figure 6. Generally, the surface manifestation and geological fault lies on medium to high density presented by yellow-red portions. The high density zones of the L_1 are widely interpreted as fracturing zones and served as geothermal fluid path to the surface. Temporal L_1 map showed the value of length density in some manifestation are different, for example, at Wayang manifestation the value of length density decreasing in time. The similar phenomenon has been occurred in the Kertamanah hot springs manifestation, except the Kawah Burung mud pool manifestation value the the L_1 increases over time.

5.5. PS-INSAR GROUND SURFACE DEFORMATION SERIES

Following spatiotemporal detection of lineament density using SAR dual orbit data, we tried to correlate with deformation series using Persistent Scattering Interferometric SAR (PS-InSAR). PS-InSAR is a method of surface deformation detection using various data pair with minimum distance of sensor acquisition (perpendicular baseline) at different times to eliminate the phase delay atmospheric effect on the deformation component at observed points. The data from Advanced Land Observing Satellite (ALOS) with Phased Array L-band type SAR (PALSAR) level 1.0 were used in this research. The amount of data needed as much as 18 scenes covering the area of Mt. Wayang Windu. Steps of the PS-InSAR processing to obtain a surface deformation value follow Berardino et al. (2002) are described as follows:

1. Evaluation of the orbital parameters associated with the SAR data acquisition time with a reference data base called the master.
2. Single View Complex Processing (SLC) SAR images are focusing signals.
3. Convert the DEM geometry position to the slant range geometry of the master data used and calculate the distance from the sensor to the target (range) for each data acquisition used.
4. Selection of the most optimal interferometric data pair with the shortest baseline perpendicular criteria.
5. Co-registration process of each SLC data pair with reference SLC master data.
6. SAR differential interferogram calculation process (D-InSAR) and coherence image creation to know the quality of interferogram produced.
7. The filtering process of D-InSAR fringes is generated.
8. Making a map of the mean value distribution of deformation velocity temporally for each pixel having high coherence with the required correction.
9. The geocoding process for each image generated from the slant coordinates to universal cartography

The results of PS-InSAR processing are depicted by Figure 7 and presented deformation maps in millimeter scale. Figure 7 showed that the variation of deformation over time time. Inflation or deflation surfaces may have correlated with the changes in surface and subsurface condition. The significant changes were located around injection well WWF and WWW. At this area the the deformation decreased in periode 2007-2008 and periode 2010-2011. On periode 2008-2009 the value of deformation increased almost all of area Wayang-Windu Geothermal Field.



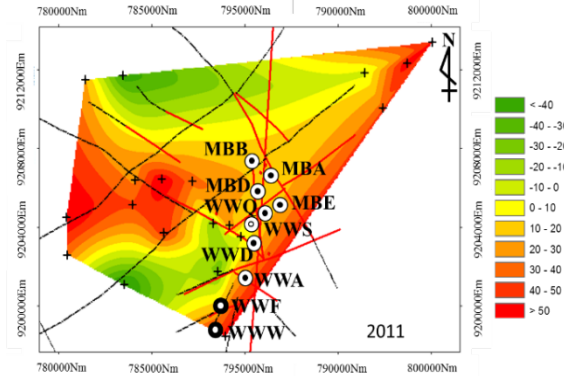


Figure 7. Time series deformation obtained from PS-InSAR method. PS points are presented by “+” symbols. Fault distributions, surface features, and wells are included in the figure.

5.6. DISCUSSION

We analyzed the temporal change of lineament density and PS-InSAR deformation at surface manifestations and production wells points. The spatiotemporal changes may indicate the dynamic of subsurface condition related to hydrothermal fluid circulation in permeable zones and steam productions. The temporal change of lineament density and PS-InSAR deformation at Kawah Burung showed similar pattern that in the early 2008 the deformation increased and followed by decreasing in middle 2009 to 2011 (Figure 8). The general temporal pattern of lineament density and deformation showed similar pattern, except small variation of lineament density in the 2007. At Kawah Wayang the similarity pattern between density and deformation were occurred in early 2009 to the end 2010 that the lineament density and deformation value increased since early 2009 to middle 2009 and followed by decrease in the end 2010 (Figure 9). At Kertamanah hot spring, the lineament density and deformation decreased in the early to the end of 2007, then increased in the end to middle 2009, and decreased again middle 2009 to beginning 2011 (Figure 10). According to temporal change of the three manifestation locations, the lineament density and deformation are concordance to increase from early 2008 until middle 2009 followed by decreasing until 2011. The change of lineament density agreed to the deformation. Figure 8 showed scatter plot of lineament density and deformation from the three geothermal manifestation including mud pools, altered surfaces, and hot springs. It may indicate that the temporal change of lineament density and deformation has occurred widely regardless surface manifestation type.

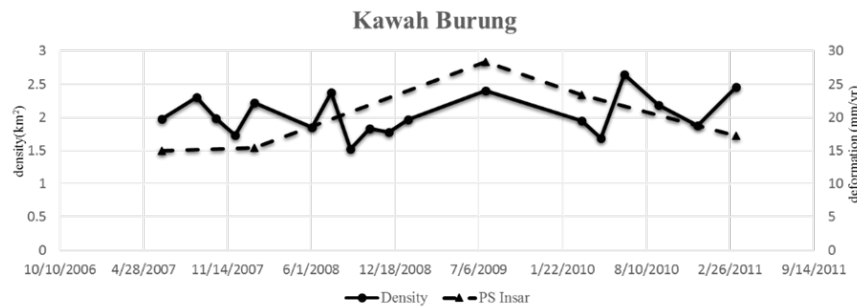


Figure 8. Scatter plot of lineament length density and PS-InSAR deformation at geothermal manifestation mud pools (Burung Crater).

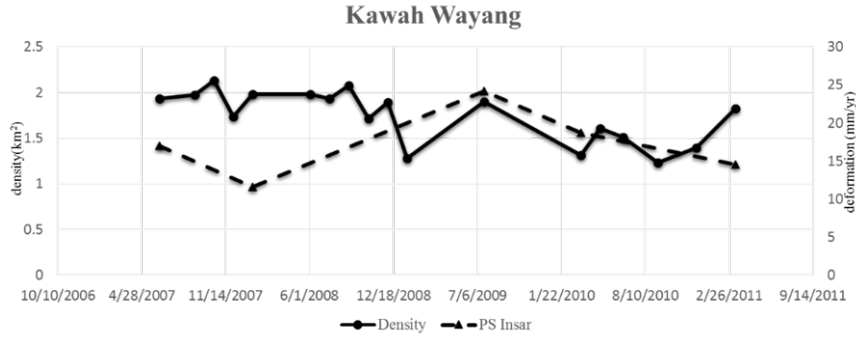


Figure 9. Scatter plot of lineament length density and PS-InSAR deformation at geothermal manifestation altered surface (Wayang Crater).

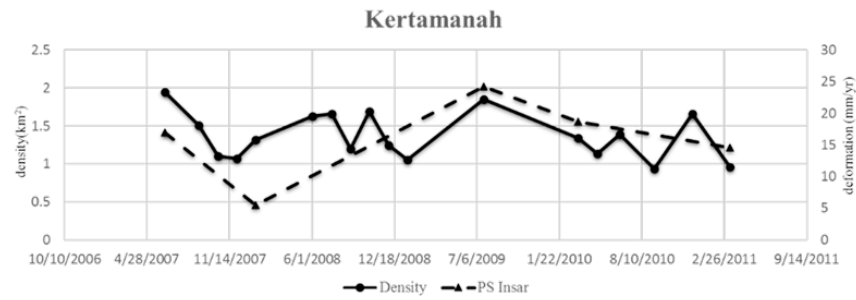


Figure 10. Scatter plot of lineament length density and PS-InSAR deformation at geothermal manifestation hot springs.

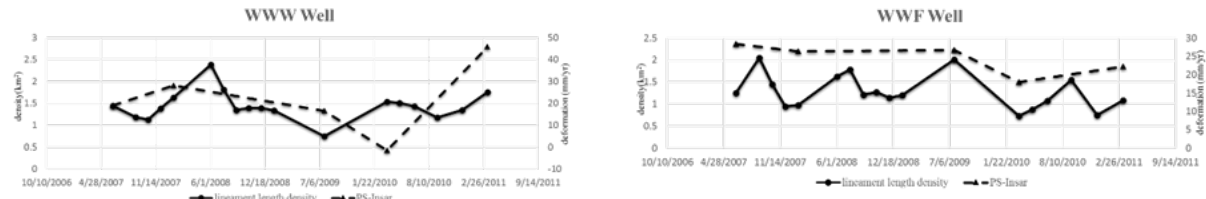


Figure 11. Scatter plot of lineament length density and PS-InSAR deformation at geothermal production wells in WWGF.

To obtain the temporal changes at geothermal wells, Figure 11-12 showed scatter plot of lineament density and PS-InSAR deformation at injection and production wells. There are two injection wells termed as WWW and WWF wells. The WWW well showed similar pattern of lineament density and deformation in 2007-2008, but in middle 2009 the lineament density and deformation are vice versa that the lineament density increase and deformation decrease (Figure 11). The WWF well showed similar pattern between lineament density and deformation that both values decrease over time in general.

Production wells in WWGF composed by 8 wells including WWS, WWQ, WWD, WWA, MBE, MBD, MBB and MBA Well. The WWS and WWQ wells are located near to each other, thus the pattern of lineament density are similar and the pattern of PS-InSAR deformation of both wells increase from 2007 to middle of 2009, then decrease to early 2010 and increase again to 2011. The WWD and WWQ wells were also showed similar pattern of deformation, but lineament density of WWD well contrary with deformation pattern. The WWA well showed similar pattern between density and deformation. But, the WWA well in middle of 2009 the lineament and deformation values are constant. The MBE and MBD wells showed different pattern between deformation and density that in the middle of 2009 the deformation increase but the lineament density decrease. For the MBB well, the deformation and lineament density

pattern showed similar, but for MBA well, the deformation pattern is vice versa with lineament density over time.

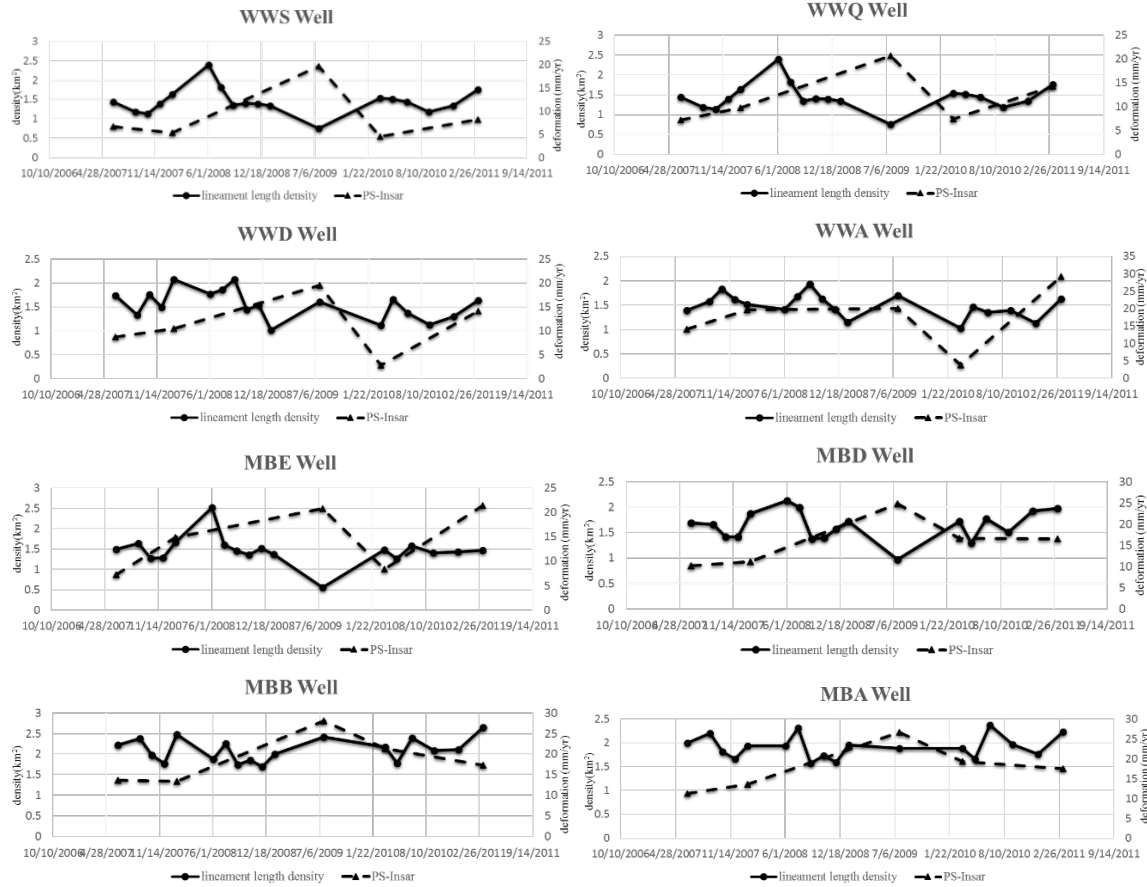


Figure 12. Scatter plot of lineament length density and PS-InSAR deformation at production well in WWGF.

5.4. CONCLUDING REMARKS

The backscattering intensity images of ALOS PALSAR in ascending and descending orbits are plausible to detect the old geological structures with plain surfaces due to long erosion. Small remaining fault landscape such as breccia will be observed as bright tone due to SAR sensitivity to the surface roughness. The rock types and thermal activities are significant to the ground surface processes. Moreover, strong thermal activities will alter the matrices of volcanic products such as lava flow and pyroclastics into high erodibility material such as clays. Then, the erosion process removes the matrices, remains the fragments of the rocks, and produces rough surfaces.

The vector summations applied to the modified Segment Tracing Algorithm (mSTA) were effective to remove the noise from double-detected lineaments of dual orbit images. The density of detected lineament after OK was used successfully to estimate the fractures permeability at ground surface. The field measurements of surface manifestation were used as criterion for high surface permeability. The surface manifestation and geological fault lies on medium to high lineament length density. The high density zones are widely interpreted as fracturing zones and served as geothermal fluid path to the surface. Temporal lineament density map showed that the length density in some manifestation are vary e.g. at altered surfaces and hot springs the value of length density decreased over time, but increased at mud pool manifestations.

According to PS-InSAR deformation, the significant inflation or deflation surfaces were occurred around production well WWF and WWW. At those wells, the deformation decreased in 2007-2008 and 2010-2011. Comparing to the deformation, both injection wells showed similar pattern of lineament density in general. The decrease and increase of lineament density are concordant with deformation. The amount of injected fluid affected to the ground surface presented by deformation and lineament density. In 2008-2009 the deformation increased almost all well in WWGF. Further investigations to the field condition are aimed to the next step for obtaining the spatiotemporal phenomena at steam production field.

1. LIST OF RESEARCH OUTPUT

6.1. International Journals:

1. Maghsoudi Y., van der Meer F., Hecker C., Perissin D., **Saepuloh A.**, Using PS-InSAR to detect surface deformation in geothermal areas of West Java in Indonesia, International Journal of Applied Earth Observation and Geoinformation, Vol. 64, pp. 386-396, doi. 10.1016/j.jag.2017.04.001, February 2018, [<http://dx.doi.org/10.1016/j.jag.2017.04.001>].
2. **Saepuloh A.**, Haeruddin H., Heriawan M.H., Kubo T., Koike K., and Malik D., Application of lineament density extracted from dual orbit of Synthetic Aperture Radar (SAR) images to detecting fluids paths in the Wayang Windu geothermal field (West Java, Indonesia), Geothermics, Vol. 72, pp. 145-155, March 2018, [<https://doi.org/10.1016/j.geothermics.2017.11.010>].

6.2. National Journals:

1. Witra T., Saepuloh A., Harto A.B., Wikantika K., Analyzing surface roughness models derived by SAR and DEM data at geothermal fields, Bulletin of Geology, Fakultas Ilmu dan Teknologi Kebumian, ITB, vol. 1, no.2, Oktober 2017.[<http://www.buletingeologi.com/index.php/buletin-geologi/article/view/11/1>]
2. Saepuloh A., Saputra R.A., Sumintadireja P., Pemetaan geologi gunungapi digital berdasarkan data reflektansi dan suseptibilitas magnetik batuan, Jurnal Geologi dan Sumberdaya Mineral (JGSM), vol. 18, no. 4, Badan Geologi, Kementerian Energi dan Sumber Daya Mineral, November 2017. [<http://jgsm.geologi.esdm.go.id/index.php/JGSM/article/view/338/298>]

6.3. International Proceedings (Scopus Index):

1. **Saepuloh A.**, Bakker E., Identifying Successive Eruption of Guntur Volcanic Complex Using Polarimetric Synthetic Aperture Radar (PolSAR) And Magnetic Susceptibility Data, IOP Conference Series: Earth and Environmental Science, Vol. 71, No. 012004, pp. 14, doi. 10.1088/1755-1315/71/1/012004, available online 27 June 2017, [<http://dx.doi.org/10.1088/1755-1315/71/1/012004>].
2. Sabrian P.G., **Saepuloh A.**, Syafrizal, Hede A.N.H., Identification of Altered Minerals Based on Synthetic Aperture Radar (SAR) For Mineral Exploration In Indonesia, IOP Conference Series: Earth and Environmental Science, Vol. 71, No. 012021, pp. 8, doi. 10.1088/1755-1315/71/1/012021, available online 27 June 2017, [<http://dx.doi.org/10.1088/1755-1315/71/1/012021>].
3. Mushoddaq M., **Saepuloh A.**, Analyses of surface deformation with SBAR InSAR method and its relationship with aquifer occurrence in Surabaya City, East Java, Indonesia, IOP Conference Series: Earth and Environmental Science, Vol. 71, No. 012010, pp. 8, doi: 10.1088/1755-

1315/71/1/012010, available online 27 June 2017, [<http://dx.doi.org/10.1088/1755-1315/71/1/012010>].

4. **Saepuloh A.**, Bakker E., The Significance of SAR Remote Sensing In Volcano-Geology For Hazard and Resource Potential Mapping, AIP Conf. Proc. Vol. 1857, No.1, pp. 070005-1 - 070005-10, doi: 10.1063/1.4947403, available online July 2017, [<http://dx.doi.org/10.1063/1.4987093>].

6.4. International Conferences:

1. Kurniawahidayati B., Nugroho I.A., Mulyana R.S., **Saepuloh A.**, Preliminary study of near surface detections at geothermal field using optic and SAR imageries, Proceeding of the 6th ITB International Geothermal Workshop 2017, Bandung, Indonesia, March 2017.
2. Nugroho I.A., Kurniawahidayati B., Mulyana R.S., **Saepuloh A.**, Preliminary determination of geothermal working area based on Thermal Infrared and Synthetic Aperture Radar (SAR) remote sensing, Proceeding of the 6th ITB International Geothermal Workshop 2017, Bandung, Indonesia, March 2017.
3. **Saepuloh A.**, Suryantini, Hecker C., Hewson R., simulating ground thermal anomaly under conditions of dense vegetation based on lab and field measurements to support thermal infrared remote sensing techniques, Proceedings The 5th Indonesia International Geothermal Convention & Exhibition (IIGCE) 2017, Jakarta Convention Center, Jakarta, August 2017.

Hecker C., Hewson R., Setianto A., **Saepuloh A.**, van der Meer F.D., Multi-source remote sensing data analysis for geothermal targeting on Flores island, Proceedings The 5th Indonesia International Geothermal Convention & Exhibition (IIGCE) 2017, Jakarta Convention Center, Jakarta, August 2017.